In-situ water-immersion experiments on amorphous silicates in the $MgO–SiO_2$ system: implications for the onset of aqueous alteration in primitive meteorites

Yohei Igami[a]*, Akira Tsuchiyama[b,c], Tomoya Yamazaki[d], Megumi Matsumoto[e], Yuki Kimura[d]

[a] Division of Earth and Planetary Sciences, Graduate School of Science, Kyoto University, Kyoto 606-8502, Japan

[b] Research Organization of Science and Technology, Ritsumeikan University, Kusatsu 525-8577, Japan

[c] Guangzhou Institute of Geochemistry, Chinese Academy of Sciences, Guangzhou, 510640, China

[d] Institute of Low Temperature Science, Hokkaido University, Sapporo 060-0819, Japan

[e] Department of Earth and Planetary Materials Science, Tohoku University, Sendai 980-8578, Japan

*Corresponding author. E-mail: y-igami@kueps.kyoto-u.jp

Abstract

Amorphous silicates, abundant in primitive carbonaceous chondrites, are among the most primitive materials from the early Solar System. They show evidence of some aqueous alteration in the meteorite parent bodies, but it is not clear how this highly reactive material changed at an early stage after contact with water. Herein, we report *in-situ* experiments on the aqueous alteration of amorphous silicate nanoparticles (typically 70 nm

in diameter); we used two different compositions that are similar to forsterite (MgO/SiO_2 = 2.02) and enstatite (MgO/SiO_2 = 1.15) in the simple $MgO–SiO_2$ system to understand basic reaction principles at the onset of the aqueous alteration. The experiments were performed in pure water at room temperature using X-ray diffraction (XRD), transmission electron microscopy (TEM), and pH measurements. The *in-situ* TEM images of the nanoparticles—in particular those with the forsterite composition—gradually became difficult to recognize in water. The pH value of the water also increased with time, suggesting that preferential Mg^{2+} dissolution occurred from the amorphous silicates right after mixing with water. The *in-situ* XRD patterns showed that magnesium silicate hydrate (M-S-H), which is a poorly crystalline phase like a phyllosilicate, newly appeared. The M-S-H seems to have been formed *via* a dissolution–precipitation process. Its formation rate from amorphous silicates was considerably higher than from crystalline silicates, because amorphous silicates are highly metastable and have high solubility in water. M-S-H formation from the forsterite composition, which has a highly unstable amorphous structure, is ten times faster than from the enstatite composition. The M-S-Hs show string-like or tiny fragmental textures in the final dried products that are very similar to those observed in the matrices of some primitive carbonaceous chondrites. M-S-H would have been the initial product formed in the aqueous alteration of amorphous silicates in the meteorites; thus, it is an important tracer of early aqueous activity at low temperatures in the early Solar System. By comparing the *in-situ* observations with those obtained after drying the experimental samples, we found two types of M-S-Hs: *epigenetic* M-S-Hs—which have a slightly Si-rich composition—formed during drying, and *syngenetic* M-S-Hs formed by *in-situ* alteration.

Carbonaceous chondrites may also contain these two types of hydrous silicates, and this should be investigated to understand the conditions for aqueous alteration in the early Solar System in more detail. The present study clearly showed the importance of Mg/Si ratio in the precursor materials, although the actual chondrites are in more complicated multi-component system. Future experiments based on the present results can extend the investigation to the system containing Fe, S, and other components as in carbonaceous chondrites.

Keywords: amorphous silicate, magnesium silicate hydrate (M-S-H), aqueous alteration, carbonaceous chondrite, in-situ experiment

1. Introduction

Based on infrared astronomical observations, most silicate dust is considered to be amorphous in the interstellar medium (Kemper 2004) and in protoplanetary disks (van Boekel et al. 2004). Therefore, amorphous silicates are believed to be a major precursor of solid materials in the Solar System. Moreover, amorphous silicates are abundantly observed in cometary dust as glass with embedded metal and sulfide (GEMS; e.g., Keller and Messenger 2011) and in some carbonaceous chondrites (e.g., Brearley 1993, Greshake 1997, Leroux et al. 2015) that experienced less aqueous alteration. The amorphous silicates in carbonaceous chondrites, even though they are mostly primitive, nevertheless show some evidence of aqueous alteration, which occurred in the parent bodies of these meteorites due to reactions between minerals—including amorphous silicates—with melted ice (*e.g.*, Abreu and Brearley 2010, Le Guillou et al. 2015a, Matsumoto et al. 2019). Therefore, the aqueous alteration of amorphous silicates is important for understanding the evolution of small bodies driven by aqueous fluids in the early Solar System. In addition, there is increasing interest in the process of aqueous alteration of amorphous silicates in various research fields, as well as in planetary science; for example, the geochemical interest in basalt weathering (e.g., Berger et al. 1987, Oelkers 2001, Oelkers et al. 2001, Schindler et al. 2019) and the industrial interest in the alteration of nuclear-waste glasses (Frugier et al. 2008, Valle et al. 2010).

Aqueous alteration of silicates in the early Solar System has been explored through experimental studies as well as by examinations of carbonaceous chondrites (e.g., Le Guillou and Brearley 2014). Although most experimental studies have focused on the

77 alteration of crystalline silicates (Nomura and Miyamoto 1998, Jones and Brearley 2006,
78 Ohnishi and Tomeoka 2007), a few studies using amorphous silicates as starting materials
79 have been reported recently. Nakamura-Messenger et al. (2011) conducted hydrothermal
80 experiments on cometary dust containing pristine amorphous silicates. Using aqueous
81 solutions with different pH values, they observed the formation of phyllosilicates similar to
82 those found in carbonaceous chondrites. Noguchi (2012) has observed similar
83 phyllosilicates in hydrothermal experiments on amorphous silicates in a CI composition
84 synthesized using the sol–gel method.

85 However, it is still unclear how these phyllosilicates formed, particularly at the low
86 temperature (*e.g.*, room temperature) at which the aqueous alteration of most carbonaceous
87 chondrites occurred (Brearley 2006). For example, it has not yet been demonstrated
88 whether the first step toward forming phyllosilicates *via* aqueous alteration is the
89 dissolution of the amorphous silicates in water, hydration of the amorphous silicates, and/or
90 some other process. It is also unclear how rapidly each process progresses (whether it
91 occurs immediately or gradually) after the silicate has been immersed in water. Recently,
92 Le Guillou et al. (2015b) conducted aqueous alteration experiments with amorphous silicate
93 with olivine composition at relatively low temperatures—90 °C and 190 °C—and they
94 found some complex alteration textures in spite of the low temperature condition and short
95 duration of the experiments (two weeks). This implies that further investigation with much
96 higher time resolution is required.

97 In addition, the samples used in previous experiments experienced not only a
98 hydrothermal process but also a subsequent drying process, because the run products were

observed after drying of the samples (*e.g.*, Nakamura-Messenger et al. 2011, Noguchi 2012, Le Guillou et al. 2015b). During the drying process, it is reasonable to expect some phases to be modified or additional phases to be formed. Any additional new phase is probably similar to, but not exactly the same as, the phases formed during the hydrothermal process. If this is the case, it is necessary to distinguish the original run products formed through aqueous alteration from those arising during the drying process. By extension, carbonaceous chondrites also may have two types of aqueous alteration products, which must be distinguished in order to understand the exact conditions of their aqueous alteration. This seems to have been overlooked in many cases until now.

In this study, we have therefore conducted *in-situ* observations of the aqueous alteration of amorphous silicates using powder X-ray diffraction (XRD) and transmission electron microscopy (TEM). We also analyzed the run products after drying. *In-situ* pH measurement of water with amorphous silicates was also made. Based on these results, we discuss the processes that occur in the very early stages of aqueous alteration and evaluate the effect of the subsequent drying process in order to facilitate the decoding of the carbonaceous chondrites.

2. Experimental methods

2.1. Starting materials

120 The samples used in the current experiments were amorphous silicates in the
121 $MgO–SiO_2$ system. We used two different chemical compositions that are similar to
122 forsterite (MgO/SiO_2 = 2.02; sample name, am-Fo) and enstatite (MgO/SiO_2 = 1.15; sample
123 name, am-En). We used the $MgO–SiO_2$ system as it is the simplest system representing
124 amorphous silicates in carbonaceous chondrites. For simplicity we excluded FeO, which is
125 another important component, because it is difficult to control the redox state of Fe in
126 *in-situ* aqueous alteration experiments. If Fe is present as FeO, some MgO in phyllosilicates
127 is replaced by FeO. In addition, amorphous silicates in GEMS are poor in FeO, and most of
128 the Fe is included as nanoparticles of metallic iron and iron sulfide.
129 The present amorphous silicate samples were synthesized in an induction thermal
130 plasma (ITP) furnace at Nisshin Flour Milling Inc. (Koike et al. 2010, Imai 2012,
131 Yamamoto and Tachibana 2018, Takigawa et al. 2019a). In this furnace, a mixture of
132 $Mg(OH)_2$ and SiO_2 powder was evaporated in a high temperature plasma (~10^4 K), and
133 spherical nanoparticles ~20–200 nm (~70 nm on average) in diameter (Figs. 1a and d) were
134 condensed from the gas by quenching at an ultra-high cooling rate (~1–10 × 10^4 K/s). Their
135 bulk chemical compositions, noted above, were determined with an electron probe
136 microanalyzer after the powders had been compressed. Scanning transmission electron
137 microscopy with energy-dispersive X-ray spectroscopy (STEM-EDS) analysis yielded
138 consistent Mg/Si ratios of 2.00(4) for am-Fo and 1.10(2) for am-En, and they displayed
139 spatial homogeneity on the nanometer scale (Figs. 1b and e). Each XRD pattern showed a
140 very broad peak corresponding to amorphous silicates, and there are no obvious peaks of
141 crystalline silicates or hydrates (Figs. 1c and f). The widths of the broad peaks were similar

142 to those of amorphous silicates used in other previous experiments (*e.g.*, Roskosz et al.
143 2011). The peak positions for am-Fo and am-En were different (~31° and ~26 ° in 2θ Cu*K*α,
144 respectively), indicating a difference in their average structures in the amorphous state. The
145 TEM-detected electron-diffraction patterns showed that almost all the observed particles
146 were amorphous (Figs.1 a and d).
147
148 **2.2. Experimental protocol**
149 We performed two types of *in-situ* experiments (Fig. 2) on the two samples
150 (am-Fo and am-En): aqueous-XRD experiments (aq-XRD) and aqueous-TEM experiments
151 (aq-TEM), which provide complementary information. From aq-XRD, we obtained powder
152 diffraction patterns of bulk samples immersed in water, using a specific XRD holder to
153 prevent water evaporation. From aq-TEM, we obtained TEM images of individual particles
154 immersed in water, with the sample placed in a TEM holder specifically designed for liquid
155 observations. After each of the two experiments, the run product was dried, and additional
156 analyses were performed on the dried products. In addition, pH measurements of water
157 mixed with amorphous silicates were also performed. All measurements were made at
158 room temperature.
159
160 **2.3. Aqueous-XRD experiment**
161 Each starting material (~0.3 g) was mixed with deionized water (~ 0.3 mL), with a
162 water/rock (W/R) ratio of approximately 1 by mass. For carbonaceous chondrites, a W/R
163 ratio as large as ~1 is estimated for the CI group, which shows advanced aqueous alteration

features (Clayton and Mayeda 1999). The sample mixture was placed in an airtight sample holder (Rigaku, 2392B101) consisting of a stainless-steel stage sealed with a Viton O-ring and a polyimide film to prevent evaporation. The XRD measurement was performed using a powder X-ray diffractometer (Rigaku Smart Lab., Kyoto University) with Ni-filtered Cu*K*α radiation (40 kV, 40 mA). The step interval for scanning was 0.05°, and the diffraction angles (2θ) ranged from 4° to 80°. The first measurement was made a few minutes after the sample had been mixed with water, and the time required for one measurement was about 30 min. Measurements were conducted repeatedly for ~48 h.

After the *in-situ* measurements, the seal was removed, and the sample in the holder was dried overnight at room temperature in a vacuum maintained with a diaphragm pump. Two types of XRD patterns were obtained for the dried sample: one included the polyimide film in order to facilitate comparison with the patterns obtained from the aqueous experiments, and the other did not include the film in order to obtain a clearer profile. Finally, the run products were transferred onto a normal C-grid and analyzed using 200-keV TEM with an EDS detector (JEOL JEM-2100F, JED-2300T, Kyoto University).

2.4. Aqueous-TEM experiment

Each starting material was mixed with deionized, ultra-pure water. Ultrasonic vibration was applied to achieve a high degree of dispersion of the amorphous silicate particles in the water. A drop of the sample mixture (<1 μL) was placed into a liquid cell in a TEM holder specifically designed for *in-situ* observations (Poseidon, Protochips Inc.) and was cautiously sealed with an ultrathin film of amorphous SiN_x, using the same procedure

as Satoh et al. (2018). (A sketch of the cell system is shown in Fig. S1 of Holtz et al. 2013 or Fig. S1 of Yamazaki et al. 2017, although the present experiment did not use a liquid-flow system). While this was ideal for performing experiments with a W/R ratio similar to those used for aq-XRD, this was impossible for the TEM holder. Thus, we adopted W/R ratios of ~10–100 by mass. The holder containing the sample was then placed in a TEM (JEOL JEM-2100F, Hokkaido University). We observed the time evolution of the samples through bright-field imaging at 200 keV for ~24 h. The electron flux was ~10^2 electrons/(s·nm^2) or less, at which no significant effects were found in previous *in-situ* liquid experiments for protein crystallization (Yamazaki et al. 2017). To suppress electron-irradiation effects on the reactions further, we sequentially and repeatedly observed several regions, avoiding continuous illumination of any one specific region. Scattering of the electron beams by water sealed with a couple of 50-nm-thick SiN_x films was so extremely large that no electron-diffraction patterns or characteristic X-ray spectra were measured. Due to unavoidable timing constraints imposed by procedures such as sample setting and sealing, the observation started approximately 30 min after the sample had been mixed with water. After the *in-situ* TEM experiment, which lasted for ~24 h, the seal was removed, and the sample in the cell was dried overnight at room temperature in a vacuum maintained with a diaphragm pump. The dried sample on the amorphous SiN_x film was then observed *via* TEM (JEOL JEM-2100F, Kyoto University).

2.5. pH measurements

Each starting material (~20 mg) was mixed with deionized water (~20 mL) at a W/R ratio of ~100 by mass, which is similar to that of the aq-TEM sample. The pH of the liquid in the mixture was repeatedly measured with a pH meter (HORIBA, LAQUAact D-75) during the two days after the moment of mixing. The samples were always covered with a plastic film to prevent water evaporation, except during the pH measurements (~1 min). We did not measure the chemical composition of the liquid, because the liquid and nanoparticles cannot be separated.

214 ## 3. Results

215 ### 3.1. Aqueous-XRD experiment

216 The time evolution of the XRD patterns obtained in the aqueous alteration
217 experiments are shown in Figs. 3a and b. The patterns of the starting materials without
218 water and of the dried products at the end of the experiment are shown respectively at the
219 bottom and top of each plot. These patterns were taken in dry conditions for samples
220 covered with a polyimide film to enable robust comparison with the *in-situ* aq-XRD results.
221 The diffraction peaks at around 43° and 51° (open triangles) correspond to the
222 stainless-steel used in the sample holder, and the broad peaks at approximately 6°, 11°, and
223 15° (open diamonds) correspond to the polyimide film used to seal the sample (Fig. 3d).
224 They do not present any significant problems for the analysis of the results. In addition, we
225 detected tiny, sharp peaks at approximately 13° (~0.68 nm) and 20° (~0.44 nm) for am-Fo
226 and at 15° (~0.59 nm) and 20° (~0.44 nm) for am-En (open squares) that cannot be
227 attributed to any reasonable phases in the Mg–Si–O–H system or carbonates. We assume
228 that these tiny peaks are negligible for the following discussion. The absence of carbonates
229 indicates that dissolution of CO_2 from the air into the water is little and it did not change
230 the pH to affect chemical reactions seriously during the experiments.

231 As aqueous alteration progressed, broad new peaks appeared at 2θ = ~35° and 60°
232 (solid circles in Fig. 3). The broadness of these XRD peaks indicates very low crystallinity,
233 and the asymmetry of the ~35° peak indicates a nanometric size and a turbostratic lamellar
234 texture (Warren 1941). These peaks can be attributed to a phyllosilicate-like hydrous phase
235 with quite poor crystallinity, named M-S-H (magnesium silicate hydrate), which is

commonly known in the cement and concrete industry, where it is used in particular for nuclear-waste encapsulation, and it also occurs in natural rocks such as clay-rich or granitic rocks (e.g., Cole 1953, Zhang et al. 2011, Dauzeres et al. 2016, Mäder et al. 2017). Previous studies reported that synthesized M-S-Hs show XRD peaks at ~7° (~9° in air-dried conditions), ~20°, ~35° (asymmetric), and ~60° (e.g., Roosz et al. 2015, Bernard et al. 2019), and similar features are also confirmed from M-S-Hs collected from interfaces between cement and natural clay (Dauzeres et al. 2016). The structure of M-S-H is not well known, but it has been correlated with talc, sepiolite, and/or serpentine group minerals (Brew and Glasser 2005, Roosz et al. 2015, Nied et al. 2016, Bernard et al. 2017, 2019). The asymmetric peak at ~35° is also confirmed in some poorly crystalline, disordered phyllosilicates as a prism reflection, and the peak at 2θ = ~60° corresponds to the 060 and/or 330 reflections from phyllosilicates.

The profiles at around 25–33°, where amorphous silicates show broad diffraction peaks (the gray arrows in Fig. 3), changed significantly during the experiments. These changes may be contributed by water (Fig. 3c) and by the M-S-H ~20° peaks, as well as by amorphous silicates. Thus, it is difficult to identify the cause of the profile change without deconvolving the pattern, as we discuss later.

3.2. Run products after aqueous-XRD experiments

Fig. 4 shows the XRD patterns of the dried run products without the airtight sample holder (the polyimide film and stainless-steel holder). In addition to the features already detected in the aq-XRD patterns (the ~25° broad peak, ~35° prism peak, and ~60°

peak), a very broad peak at 2θ = 9°, which corresponds to the basal-plane reflection of M-S-H, was detected in am-Fo (Fig. 4a, inset). This position is similar to talc, one of the Mg phyllosilicates [$Mg_3Si_4O_{10}(OH)_2$], although the peak is weak and very broad, indicating disordered stacking. In contrast, no clear signature of basal-plane reflection was observed in am-En, but a very broad increase in intensity around 2θ = 5–11° can be recognized by comparison with the blank measurement pattern (Fig. 4b, dotted line in the inset panel). This highly-diffused basal diffraction indicates that the degree of the stacking order is extremely low.

TEM images of dried aq-XRD samples are shown in Fig. 5. The am-Fo particles have almost lost their original spherical shapes and have formed aggregates of string-like materials (Fig. 5a). In contrast, the am-En particles more-or-less maintained their original spherical shapes (Fig. 5d), and fine objects rather than string-like materials were found around the particles. Both may correspond to M-S-H. High-resolution TEM images of the M-S-Hs (lower right images in Figs. 5a and d) show no clear lattice fringes, indicating extremely poor crystallinity, which corresponds to the very broad XRD pattern (Fig. 4). The selected-area electron-diffraction (SAED) patterns of both samples feature rings (Figs. 5b and e). They show peaks suggesting ~0.25 nm and ~0.15 nm in *d*-spacing, corresponding to the XRD peaks at 35° and 60° in Fig. 4, respectively.

STEM-EDS analysis of the products yields the average Mg/Si ratios of 2.04(3) for am-Fo and 1.04(3) for am-En, suggesting that the average compositions changed very little, if at all, from the starting materials. However, the STEM-EDS imaging exhibits spatial heterogeneity of the Si/ (Si + Mg) ratio at the nanometer scale (Figs. 5c and f). In both

samples, the particle surfaces seem to be enriched in Si. This seems to correspond to the string-like materials or fine objects and probably precipitated from liquid during drying, as also described later.

3.3. Aqueous-TEM experiment

To obtain nanometer scale images of particles during aqueous alteration, we performed *in-situ* TEM observations for water-immersed silicate particles (Fig. 6). As time passed, the aq-TEM images gradually became blurred throughout the whole image, and thus particles became difficult to recognize clearly in the liquid. This is probably due to an increase in the electron-scattering power of the aqueous solution caused by cation dissolution from the silicates into the water. Although the particle sizes in the aq-TEM images appear to be larger than those of the starting material (particularly for am-Fo, Fig. 6a), this is probably only an apparent expansion caused by a combination of particle clustering and image blurring. The expansion may also reflect hydration of individual particles, but it is difficult to determine whether it really occurs from the aq-TEM images alone. The blurring seems to progress faster for am-Fo (Fig. 6a) than for am-En (Fig. 6b). The change in particle appearance is recognized more easily for am-En. Final *in-situ* aq-TEM images after the elapse of almost a day are shown at the bottom of Fig. 6 and in Figs. 7a and c. These images show that the boundaries between particles and liquids are barely recognizable for both am-Fo and am-En.

3.4. Run products after the aqueous-TEM experiments

Figs. 7b and d show TEM images and SAED patterns of the two run products after drying. The dark objects observed in Figs. 7a and c likely correspond to particles that are seen clearly in Figs. 7b and d. The textures of the dried products from am-Fo (Fig. 7b) are almost the same as those of the aq-XRD products (Fig. 5a), whereas the am-En particles (Fig. 7d) maintained their sphericity to a higher degree than those of aq-XRD (Fig. 5d). On the SiN_x film, aggregates of string-like materials for am-Fo (Fig. 7b lower right) and small irregular objects a few tens of nm in size for am-En (Fig. 7d lower right) were observed. They were likely the same materials as those attached around the particles and were likely precipitated from the liquid. High-resolution TEM images of the aq-TEM products were not obtained, because they were less clear due to the background caused by the 50-nm-thick amorphous SiN_x film used as the bottom floor of the sample holder for aq-TEM.

3.5. pH measurements

Fig. 8 shows the results of the pH measurements. This clearly shows that the pH value of the liquid became high in the beginning, suggesting preferential Mg^{2+} dissolution from the silicates into the water. This is consistent with previous studies (Chizmadia and Lebrón-Rivera 2010, Hellmann et al. 2012, Ruiz-Agudo et al. 2014, Gin et al. 2015) and indicates that the blurring observed in aq-TEM was mainly caused by this dissolution. The pH value reached a maximum right after mixing for am-Fo and in ~2 hours after mixing for am-En (Fig. 8, inset). The pH value then decreased gradually, probably due to subsequent

Si^{4+} (SiO_4^{4-}) dissolution and the precipitation of M-S-H, consuming the Mg^{2+} in the solution. After two days, the pH value still remained higher than 9.

4. Discussion

4.1. XRD peak deconvolution

For quantitative evaluation, peak-fitting was conducted for the series of aq-XRD profiles (a typical fitting result is shown in Fig. 9). The profiles in the range 2θ = 10–55° were fitted by a combination of diffraction peaks due to the polyimide film, amorphous silicates, M-S-H, and liquid, with a background assumed to be linear (Fig. 9a). The polyimide diffraction peak (10°) and the amorphous peak (~25°) were fitted with Voigt functions, and the M-S-H prism peak (~35°) was fitted with an asymmetric split Voigt function. The diffraction profile of the liquid was assumed to be the same as that of water (Fig. 3c). Because the water diffraction profile was well fitted with two Voigt functions, the liquid diffraction was fitted with the same two Voigt functions, with only the scale factor adjusted. The polyimide peak at ~6° and the M-S-H peak at ~60° are out of the range 2θ = 10–55° and do not overlap with any other peaks. Thus, they were fitted individually after subtracting a linear background (Figs. 9b and c).

All the aq-XRD patterns were well fitted with a superposition of the above functions, yielding respective peak intensities from all the patterns. Fig. 10 shows the time evolution of the integrated peak intensities of the liquid, M-S-H (prism and ~60°), and amorphous silicates after normalization to the intensity of the polyimide ~6° peak, which should be constant during each experiment. The peak intensities of the M-S-H prism (Figs. 10b and f) and ~60° peaks (Figs. 10c and g) increase with time in a similar way for both am-Fo and am-En, and the curves for these intensity increases are roughly complementary to those of the liquid (Figs. 10a and e) and the amorphous silicates (Figs. 10d and h). The

peak intensity of the liquid did not drop to zero until the samples were vacuum dried. It should be noted that the intensity of the amorphous silicates may not be accurate, because several peaks overlap in the 2θ region around 25–33°, and some other peaks which were not used in the present fitting—such as the M-S-H ~20° peak (e.g., Roosz et al. 2015, Bernard et al. 2019)—may exist in this region as well.

4.2. Aqueous alteration processes in the earliest stage

4.2.1 The process controlling M-S-H formation

The selective dissolution of Mg^{2+} followed by Si^{4+} (SiO_4^{4-}) dissolution, as indicated by the pH measurement (Fig. 8), is consistent with the Si–O bond energy being significantly higher than the Mg–O bond energy (Huggins and Sun 1946). This would make the diffusion coefficient of Mg^{2+} higher than that of Si^{4+} in the amorphous silicates. Moreover, the amorphous silicates are in a highly metastable state, and thus their solubilities should be larger than that of M-S-H, which is comparable with the solubilities of Mg phyllosilicates (Bernard et al. 2017). This should cause overshoot of the Mg^{2+} and Si^{4+} dissolution, to the extent that their solubility product becomes much higher than that for phyllosilicates and M-S-H. From the highly supersaturated solution, highly disordered M-S-Hs should be formed, rather than the more-stable crystalline phases. A similar dissolution–precipitation process has been proposed to be mostly dominant for general mineral–fluid reactions as well (Hellmann et al. 2012, Ruiz-Agudo et al. 2014, Gin et al. 2015), but there may be great differences in the dissolution rates. In altering amorphous

371 silicates, very rapid dissolution produces a supersaturated solution and the formation of a
372 characteristic M-S-H with a highly disordered structure.
373 We observe some diffraction intensity from amorphous silicates even at the end of
374 the experiments (Figs. 10d and h). This suggests the existence of amorphous silicate
375 remnants, which should be more-or-less hydrated. Assuming that the hydration rate is
376 controlled primarily by the diffusion of water molecules into the amorphous silicates, we
377 roughly estimated the degree of hydration. By extrapolating experimental results of the
378 diffusion coefficient of water (D_{H_2O}) in amorphous silica (Wakabayashi and Tomozawa
379 1989) to room temperature, a diffusion distance in 1 hour (t = 1 h) is estimated to be ~15
380 nm, which corresponds to a volume fraction of ~80% for spherical particles with the
381 diameter of 70 nm. Because D_{H_2O} in am-Fo and am-En should be larger than that in
382 amorphous silica, it is reasonable that hydration would have occurred in a few hours or less
383 after contact with water in the current experiments. Figs. 10a shows that the water intensity
384 decreases before the formation of M-S-H in am-Fo. This also suggests that amorphous
385 silicate particles not only were dissolved into the water to form M-S-H but also were
386 hydrated.
387
388
389 *4.2.2 Rate equation for M-S-H formation*
390 We have estimated the M-S-H formation rate using the deconvolved XRD peak
391 intensities of the M-S-H peaks (shown in Figs. 10b, c, f, and g). We adopted a simple

first-order equation as an empirical model, expressing the M-S-H peak intensity as a function of time *t* as

$$I(t) = I_0[1 - \exp\{k(t - t_0)\}], \quad (1)$$

where I_0 is the final intensity, k is the rate constant, and t_0 is the time delay to the start of M-S-H formation.

Using this empirical equation, good fits were obtained, as shown in Figs. 10b, c, f, and g (solid lines), yielding the fitting parameters shown in the figures. The fitted results for the prism peak and the ~60° peak are almost the same. The delay time t_0 ~ 1 h for am-Fo is clearly smaller than t_0 ~ 4–8 h for am-En. This difference is comparable to the difference in the time for the water solution to reach the highest pH values: ~10 min for am-Fo and ~2 hours for am-En (Fig. 8). The highest pH value represents the high Mg^{2+}-dissolved state, and subsequent Si^{4+}(SiO_4^{4-}) dissolution should be delayed. The delay time t_0 therefore can be interpreted roughly as the time for the water solution to reach a sufficiently high degree of supersaturation for M-S-H formation (*e.g.*, the maximum solubility product).

The rate constant k for am-Fo (~0.3–0.4 h^{-1}) is about 10 times higher than for am-En (~0.01–0.02 h^{-1}). Therefore, the degree of M-S-H formation (I/I_0), reaches ~90 % after only 7–9 hours for am-Fo, whereas for am-En the time for a 90% of the M-S-H to form requires ~140–230 h (5–10 days). The difference in k is likely related to the difference in the degree of supersaturation, which is the driving force for precipitation. The shorter t_0 and larger k for am-Fo than for am-En are both related to its more rapid

413 dissolution, which is probably due to the unstable structure of am-Fo, where polymerization
414 of the SiO_4 tetrahedron is essentially absent (Kohara et al. 2004).

415 This equation is applicable only for conditions with a sufficient amount of water
416 and with a W/R ratio roughly larger than 1. This may be reasonable if we consider the water
417 content in Mg phyllosilicates (e.g., 18.8, 17.9, 13.0, and 4.8 wt.% H_2O in saponite,
418 vermiculite, serpentine, and talc, respectively). The peak-fitting results (Figs. 10a and d)
419 also indicate that water is actually present even in the final stage of the experiments. Thus,
420 assuming that the function $I(t)$ is adequate for a W/R ratio of ~1 and higher, it can be
421 applied to the results from aq-TEM as well as to those from aq-XRD. The degree of M-S-H
422 formation in the products of am-Fo after aq-XRD (~48 h) and aq-TEM (~24 h) are both
423 estimated to be I/I_0 > 99.9 %. On the other hand, the values of I/I_0 for the am-En
424 products are estimated to be much lower. For am-En, the I/I_0 values from the aq-TEM
425 and aq-XRD products estimated from eq.(1) are ~17% at t ~ 19 h and ~43% at t ~ 40 h,
426 respectively. These values are consistent with the textures observed by TEM. The TEM
427 images of the am-Fo products showed that they have almost lost their original spherical
428 shapes, whereas the am-En products have not. Moreover, for am-En the sphericity is almost
429 preserved in aq-TEM (Fig. 7d) compared to aq-XRD (Fig. 5d).
430
431
432 **4.3. Structural variation of the M-S-H**
433 To detect changes in the M-S-H structure in detail, we focused on the M-S-H peak
434 at ~60°, which does not overlap with other peaks. Fig. 11 shows the time evolution of the

435 peak-top position, with the FWHM determined by the split Voigt function. There are clear
436 differences between am-Fo and am-En. The FWHM of am-En is larger than that of am-Fo,
437 indicating that the M-S-H from am-En has poorer crystallinity than that from am-Fo.
438 Moreover, the difference in the 2θ positions of am-Fo and am-En reflects a difference in the
439 M-S-H structures. Similarly to Mg phyllosilicates, M-S-H is expected to be composed of
440 two basic components in the crystal structure: a sheet of triple-edge-sharing MgO_6
441 octahedra (Mg^O sheet) and a sheet of corner-sharing SiO_4 tetrahedra (Si^T sheet). The *b*-axis
442 length of the single Mg^O sheet is assumed to be ~0.944 nm by reference to that of brucite
443 [$Mg(OH)_2$], which consists of Mg^O sheets alone (Ma et al. 2013), whereas the *b*-axis length
444 of the single Si^T sheet is assumed to be ~0.916 nm, based on the mean Si–O bond distance
445 of 0.162 nm (e.g., Jones 1968). These two *b*-axis lengths (~0.944 and ~0.916 nm)
446 correspond to 060 reflection peaks at 2θ values of ~58.7° and ~60.7°, respectively (Fig. 11,
447 red and blue lines). Our XRD results show that the M-S-H peaks are located at about 59–
448 60°, between those of the Mg^O and Si^T sheets. The difference in the *b*-axis lengths of the
449 M-S-H may correspond to different proportions of randomly stacked Mg^O and Si^T sheets.
450 The XRD patterns of M-S-H in a recent study (Bernard et al. 2019) also shows a consistent
451 trend in the peak position change with variations in the Mg/Si ratio. Although there should
452 be large number of in-sheet defects in M-S-H as well as stacking disorder, the assumption
453 seems roughly available. In contrast, such variations do not occur in crystalline Mg
454 phyllosilicates; they have almost constant *b*-axis lengths of ~0.92 nm and 060/330
455 reflections at ~60–61°, regardless of the Mg/Si ratio. This is because crystalline Mg
456 phyllosilicates require almost the same mesh size (*a*- and *b*-axis lengths) for Si^T and Mg^O

457 sheets; this size is close to that of the Si^{T} sheet, which is stiffer than the Mg^{O} sheet. The
458 length of the M-S-H *b*-axis varies, probably due to its very low crystallinity and structural
459 flexibility. The present results (Fig. 11) implies that the M-S-H in the am-Fo experiment has
460 a more Mg-rich composition (more abundant in the Mg^{O} sheet) than that in the am-En
461 experiment and that the structure of M-S-H in am-Fo may be more similar to brucite than to
462 silicates.

463 The 2θ peak position changed slightly during the experiments, particularly in the
464 early stage of M-S-H formation (~3 h) for am-Fo and after drying. Assuming that the
465 structural changes did not occur after precipitation, the peak position change can be
466 attributed to changes in the structure of the precipitating M-S-H. The lower peak position of
467 the first M-S-H implies that the supersaturated solution has a high Mg content, which is
468 consistent with the selective dissolution of Mg into the water during the first stage. The
469 peak shifts to higher 2θ during drying of both samples, indicating that the M-S-H that
470 precipitated during drying has a more Si-rich composition than that formed during aqueous
471 alteration. The Si^{4+} dissolved in water may have precipitated in larger quantities during the
472 drying process. This compositional change is recorded as the Si-rich rims on the M-S-H
473 particles in the STEM-EDS images (Figs. 5c and f). The present results indicate that there
474 exist two types of M-S-H: *syngenetic M-S-H*, which appears during the aqueous alteration
475 process, and *epigenetic M-S-H* that arises during the drying process. There is a high
476 possibility that the *c*-axis length (basal-plane spacing) may also be different between the
477 two types, although this could not be confirmed from the *in-situ* XRD patterns.
478

4.4. Implications for planetary science

4.4.1. M-S-H in primitive carbonaceous chondrites

Carbonaceous chondrites are subdivided into multiple classes (CB, CI, CH, CK, CM, CO, CR, and CV). Among them, the CI chondrites received the highest degree of aqueous alteration. The CM and CR chondrites generally suffered high degrees of aqueous alteration as well, with most of the water stored as hydrous phyllosilicates, mainly in the matrix (*e.g.*, Tomeoka and Buseck 1988, Bunch and Chang 1980, Weisberg et al. 1993, Tomeoka and Buseck 1985, Zolensky et al. 1993). However, some CM and CR chondrites contain primitive amorphous silicates that have likely survived aqueous alteration (Abreu and Brearley 2010, Le Guillou and Brearley 2014, Leroux et al. 2015, Chizmadia and Brearley 2008). Similar matrices of primitive nature were observed also in the ALH77307 CO chondrite (Brearley 1993) and in the ungrouped carbonaceous chondrite Acfer 094 (Greshake 1977, Matsumoto et al. 2019). These chondrites are termed "primitive carbonaceous chondrites." In previous investigations of such primitive carbonaceous chondrites, phases like poorly crystallized layered silicates with broad-ring SAED patterns have been reported (e.g., Leroux et al. 2015; Matsumoto et al. 2019). These phases must be the same as the M-S-H identified in our experimental products, and which was produced from amorphous silicates by a dissolution–precipitation process in the early stage of aqueous alteration. This is an important phase for indicating the earliest aqueous alteration

501 at low temperatures, and it should be distinguished from amorphous silicates or
502 well-crystallized phyllosilicates.

503 We consider the possibility that M-S-H can be a precursor material for some
504 crystalline phyllosilicates commonly observed in aqueously altered carbonaceous
505 chondrites. From the structural viewpoint, phyllosilicates can be formed by subsequent
506 maturing of the M-S-H, if it is heated at slightly higher temperatures. The structural
507 variation in M-S-H—which corresponds to a variable ratio of Mg^{O} to Si^{T} sheets and to the
508 degree of order in their stacking sequence—may contribute to the fine textures or defects of
509 the phyllosilicate, because the structure of phyllosilicate is essentially characterized by the
510 type of unit layer. Serpentine has a 1:1 unit layer (composed of 1 Si^{T} and 1 Mg^{O} sheet),
511 whereas talc/smectite/vermiculite has a 2:1 unit layer (composed of 2 Si^{T} and 1 Mg^{O} sheet).
512 In particular, mixed-layer phyllosilicates such as serpentine–smectite have been reported in
513 extreme aqueously altered carbonaceous chondrites (*e.g.*, Tomeoka and Buseck 1988). The
514 M-S-H in our products has a broad and low-intensity basal-plane reflection in the XRD
515 patterns (Fig. 4). This can be interpreted as the overlap of several broad peaks from various
516 basal planes. The M-S-H may transform into mixed-layer phyllosilicates or
517 well-crystallized phyllosilicates, depending on subsequent alteration conditions.

518

519 *4.4.2. Significance of amorphous silicates as primary materials for carbonaceous*
520 *chondrites*

521 As described in section 4.2.1, the disordered structure of M-S-H is attributed to the
522 highly metastable state of the precursor silicates. Therefore, the presence of M-S-H is

523 important as a tracer of early aqueous activity for primitive carbonaceous chondrites, in
524 which the matrices originally consisted of amorphous silicates.

525 Moreover, the formation rate of phases aqueously altered from amorphous silicates
526 is significantly faster than that from crystalline silicates. For example, when enstatite was
527 used as a starting material, serpentine formed in pure water only at high temperature
528 (300°C) and after a long period (>168 h), and serpentine and saponite formed only at high
529 temperature (300°C) in water with a high pH value, which was obtained by artificially
530 adding NaOH (pH = 14; Ohnishi and Tomeoka 2007). In contrast, extremely rapid
531 formation of M-S-H in water with high pH values (Fig. 8), which was obtained by the
532 dissolution of amorphous silicates into pure water at room temperature, was observed in the
533 present experiments (Fig. 10). The aqueous alteration of CM and CI chondrites have been
534 suggested to have occurred at similar low temperature conditions: <100 °C for most CM
535 chondrites (*e.g.*, Clayton and Mayeda 1999, Guo and Eiler 2007) and at ~50 °C (Leshin et
536 al. 1997) to ~150 °C (Clayton and Mayeda 1999) for CI chondrites. Therefore, a large part
537 of the hydrous phyllosilicates found in CM and CI chondrites may have been formed
538 through M-S-H from the amorphous silicates.

539 In the actual carbonaceous chondrites, Fe and/or S are also important for the
540 hydrous phases such as PCP/tochilinite-cronstedtite interlayer (Tomeoka and Buseck 1985).
541 In particular, some studies have suggested that FeO may have the effect of suppressing
542 aqueous alteration, although the process seems not so simple (Chzmadia et al. 2006,
543 Chizmadia and Lebrón-Rivera 2010, Chizmadia et al. 2011). Further investigation in the

system containing Fe and S using the present methods is required for a more comprehensive understanding of the aqueous alteration of carbonaceous chondrites.

4.4.3. Two different generations of hydrous phases

The present results strongly suggest the presence of two different generations of M-S-H: *syngenetic M-S-H* and *epigenetic M-S-H*. Similarly, two different generations may exist not only for M-S-H but also for other hydrous phases, such as crystalline phyllosilicates in general, and they might be preserved in carbonaceous chondrites. Because the two types should have slightly different compositions and/or structures, at least at the time of the formation, it may be possible to discriminate between them by careful analysis. The *syngenetic* phases should be examined selectively to understand the exact conditions for aqueous alteration. The *epigenetic* phases that arises during the drying process may effectively reflect the trace-element composition of the aqueous fluid. This will be important particularly to interpret the experimental products simulating the aqueous alteration in future studies.

4.5. Implications for cement manufacturing

M-S-H also has been a topic of interest due to its potential use in low-pH cements, *e.g.*, for nuclear-waste encapsulation (*e.g.*, Zhang et al. 2011, Dauzeres et al. 2016, Mäder et al. 2017). As shown in the present study, M-S-H phases formed by different methods and different processes may have different properties because of the diversity in their chemical

566 compositions and detailed structures, although this is still unresolved (*e.g.*, Roosz et al.
567 2015). These diversities are expected to provide the potential for designing more efficient
568 materials. The present study is the first to point out clearly that the M-S-H known in the
569 cement industry is extremely similar to the silicate ubiquitously found in primitive
570 carbonaceous chondrites, which has been called various terms such as amorphous material,
571 nanocrystalline material or very poorly crystalline material (Brealy 1993, Leroux et al.
572 2015, Chizmadia and Brearley 2008, Matsumoto et al. 2019).

573 This study also showed that M-S-H can be formed rapidly by aqueous alteration of
574 amorphous silicates. In addition, the ITP method easily can be used to form amorphous
575 silicate nanoparticles with different chemical compositions, not only in the system MgO–
576 SiO_2 but also in multi-component systems that include a variety of cations (*e.g.*, Kim et al.
577 2017, Takigawa et al. 2019b). This may provide a procedure for manufacturing different
578 varieties of silicate hydrates such as M-S-H and C-S-H (calcium silicate hydrate).

579

580

581 **5. Conclusions**

582 *In-situ* water-immersion experiments on amorphous silicates using the MgO–SiO_2
583 system were conducted to elucidate the onset processes of aqueous alteration recorded in
584 carbonaceous chondrites. The aq-TEM images showed gradual blurring probably due to
585 cation dissolution from the silicates into the water. The supplemental pH measurements
586 suggested that Mg^{2+} was dissolved immediately after the silicates were mixed with water
587 and then Si^{4+} was dissolved, which is consistent with the aq-TEM results. After the rapid

588 dissolution process, a phyllosilicate-like phase with extremely low crystallinity was
589 generated, which was identified as M-S-H (*e.g.*, Cole 1953, Zhang et al. 2011, Brew and
590 Glasser 2005, Roosz et al. 2015, Nied et al. 2016, Bernard et al. 2017, 2019) by
591 investigating the aq-XRD patterns.

592 The M-S-H was observed *via* TEM in the dried run products after the aqueous
593 experiments as string-like or tiny fragmental materials. Their appearance is very similar to
594 that of the silicates that have been observed in some primitive carbonaceous chondrites and
595 described as slightly hydrated phases like poorly crystallized phyllosilicates (*e.g.*, Leroux et
596 al. 2015, Matsumoto et al. 2019). These phases also must be M-S-H or related phases. The
597 M-S-H should exist ubiquitously in primitive carbonaceous chondrites, and it is important
598 as a tracer of the earliest aqueous activity in the early Solar System.

599 The M-S-H formation can occur within a day, even in pure water at room
600 temperature, which is significantly faster than the alteration of crystalline silicates. This is
601 due to the high metastability of the amorphous silicate. Moreover, the solubility of
602 amorphous silicates in water is much larger than that of M-S-H or phyllosilicates, causing
603 overshoot of the dissolved Mg^{2+} and Si^{4+} concentrations, followed by precipitation of
604 highly disordered M-S-Hs that are metastable, rather than stable crystalline phases, from
605 highly supersaturated solutions with high pH. This dissolution–precipitation process may
606 be the major process of aqueous alteration for amorphous silicates.

607 The M-S-H formation rate for am-Fo is about ten times higher than that for am-En.
608 This is ascribed to the difference in solubility in water, which is caused in turn by the
609 difference in thermodynamic stability of their original amorphous structure. This indicates

610 that the aqueous alteration rate depends largely on the composition/structure of the original
611 amorphous silicate, particularly at the W/R ratio of ~1.

612 Finally, the present results strongly suggest the presence of two different
613 generations of M-S-H: *syngenetic M-S-H* and *epigenetic M-S-H*. The *epigenetic M-S-H* is
614 generated by the drying process. The two types of aqueous alteration products—not only of
615 M-S-H but also of other hydrous phases—may coexist in carbonaceous chondrites. Thus,
616 they must be distinguished in order to understand their formation histories accurately. In
617 this study, the *epigenetic M-S-H* has a slightly more Si-rich composition than the
618 *syngenetic* one. It may also be possible to evaluate them selectively in carbonaceous
619 chondrites by future careful analyses.

620

621

622 **Acknowledgments**

623 We are grateful to Dr. Hisao Satoh of Mitsubishi Materials Corporation and Dr. Tsutomu
624 Sato of Hokkaido University for their discussion in terms of cement and concrete materials.
625 We are grateful to Dr. Tanya Peretyazhko of NASA Johnson Space Center for her
626 suggestions. We thank Dr. Hiroshi Hidaka of Nagoya University for his help for the pH
627 measurement. We appreciate insightful comments that improved this manuscript by
628 anonymous reviewers. The English in the manuscript was checked by Enago
629 (www.enago.jp). This work was supported by JSPS KAKENHI Grant Numbers 15H05695
630 and 20H00205. A.T. is grateful to International Fellowship for Visiting Scientists (Grant

631 No.2019VCA0004) by Chinese Academic Science at Guangzhou Institute of
632 Geochemistry.
633

References

Abreu N. M. and Brearley, A.J. (2010) Early solar system processes recorded in the matrices of two highly pristine CR3 carbonaceous chondrites, MET 00426 and QUE 99177. *Geochim. Cosmochim. Acta* **74**, 1146–1171.

Berger G., Schott J. and Loubet M. (1987) Fundamental processes controlling the first stage of alteration of a basalt glass by seawater: an experimental study between 200° and 320°C. *Earth Planet. Sci. Lett.* **84**, 431–445.

Bernard E., Lothenbach B., Rentsch D., Pochard I. and Dauzeres A. (2017) Formation of magnesium silicate hydrates (M-S-H). *Phys. Chem. Earth* **99**, 142–157.

Bernard E., Lothenbach B., Chlique C., Wyrzykowski M., Dauzeres A., Pochard I. and Cau-Dit-Coumes C. (2019). Characterization of magnesium silicate hydrate (MSH). *Cement Concrete Res.* **116**, 309–330.

Brearley, A. J. (1993). Matrix and fine-grained rims in the unequilibrated CO3 chondrite, ALHA77307: Origins and evidence for diverse, primitive nebular dust components. *Geochim. Cosmochim. Acta* **57**, 1521–1550.

Brearley A. J. (2006) The action of water. In *Meteorite and the Early Solar System II* (eds. D. S. Lauretta and H. Y. McSween). University of Arizona Press, Tucson. pp. 587–624.

Brew D. R. M. and Glasser F. P. (2005). Synthesis and characterisation of magnesium silicate hydrate gels. *Cement Concrete Res.* **35**, 85–98.

654 Bunch T. E. and Chang S. (1980) Carbonaceous chondrites—II. Carbonaceous chondrite
655 phyllosilicates and light element geochemistry as indicators of parent body
656 processes and surface conditions. *Geochim. Cosmochim. Acta* **44**, 1543–1577.
657 Chizmadia L. J. and Brearley A. J. (2008) Mineralogy, aqueous alteration, and primitive
658 textural characteristics of fine-grained rims in the Y-791198 CM2 carbonaceous
659 chondrite: TEM observations and comparison to ALHA81002. *Geochim.*
660 *Cosmochim. Acta* **72**, 602–625.
661 Chizmadia L. J. and Lebrón-Rivera S. A. (2010) Temperature and pH changes associated
662 with the hydration of amorphous silicate smokes. *Lunar Planet. Sci. Conf. XXXXI.*
663 #2536 (abstr.).
664 Chizmadia L. J., Nuth III J. A. and Rietmeijer F. J. M. (2006) Experimental aqueous
665 alteration of amorphous silicate smokes. *Lunar Planet. Sci. Conf. XXXVII*. #2187
666 (abstr.).
667 Chizmadia L. J., Santiago-Soto W. and Lebron-Rivera S. A. (2011) Exploring the
668 relationship between Fe:Si and smoke: water ratios during aqueous alteration of
669 amorphous Fe-silicate smokes. *Lunar Planet. Sci. Conf. XXXXII*. #2156 (abstr.).
670 Clayton R. N. and Mayeda T. K. (1999) Oxygen isotope studies of carbonaceous chondrites.
671 *Geochim. Cosmochim. Acta* **63**, 2089–2104.
672 Cole W. F. (1953) A crystalline hydrated magnesium silicate formed in the breakdown of a
673 concrete sea-wall. *Nature* **171**, 354–355.

674 Dauzeres A., Achiedo G., Nied D., Bernard E., Alahrache S. and Lothenbach B. (2016)
675 Magnesium perturbation in low-pH concretes placed in clayey environment—solid
676 characterizations and modeling. *Cement Concrete Res.* **79**, 137–150.
677 Frugier P., Gin S., Minet Y., Chave T., Bonin B., Godon, N., Lartigue J. E., Jollivet P.,
678 Ayral A., De Windt L. and Santarini, G. (2008) SON68 nuclear glass dissolution
679 kinetics: current state of knowledge and basis of the new GRAAL model. *J. Nucl.*
680 *Mater*. **380**, 8–21.
681 Gin S., Jollivet P., Fournier M., Angeli F., Frugier P. and Charpentier T. (2015) Origin and
682 consequences of silicate glass passivation by surface layers. *Nat. commun.* **6**, 6360.
683 Greshake A. (1997) The primitive matrix components of the unique carbonaceous chondrite
684 Acfer 094: A TEM study. *Geochim. Cosmochim. Acta* **61**, 437–452.
685 Guo W. and Eiler J. M. (2007) Temperatures of aqueous alteration and evidence for
686 methane generation on the parent bodies of the CM chondrites. *Geochim.*
687 *Cosmochim. Acta* **71**, 5565–5575.
688 Hellmann R., Wirth R., Daval D., Barnes J. P., Penisson J. M., Tisserand D., Epicier T.,
689 Florin B. and Hervig R. L. (2012) Unifying natural and laboratory chemical
690 weathering with interfacial dissolution–reprecipitation: a study based on the
691 nanometer-scale chemistry of fluid–silicate interfaces. *Chem. Geol.* **294**, 203–216.
692 Holtz M. E., Yu Y., Gao J., Abruña H. D. and Muller D. A. (2013) In situ electron
693 energy-loss spectroscopy in liquids. *Microsc. Microanal.* **19**, 1027–1035.
694 Huggins M. L. and Sun K. H. (1946) Energy additivity in oxygen-containing crystals and
695 glasses. *J. Phys. Chem.* **50**, 319–328.

696 Imai Y. (2012) Experimental study of circumstellar silicate dust evolution by crystallization
697 processes using laboratory infrared spectroscopy. Ph. D. thesis, Osaka Univ.
698 Jones J. B. (1968) Al–O and Si–O tetrahedral distances in aluminosilicate framework
699 structures. *Acta Crystallogr*. **24**, 355–358.
700 Jones C. L. and Brearley A. J. (2006) Experimental aqueous alteration of the Allende
701 meteorite under oxidizing conditions: Constraints on asteroidal alteration. *Geochim.*
702 *Cosmochim. Acta* **70**, 1040–1058.
703 Keller L. P. and Messenger S. (2011) On the origins of GEMS grains. *Geochim.*
704 *Cosmochim. Acta* **75**, 5336–5365.
705 Kemper F. Vriend W. J. and Tielens A. G. G. M. (2004) The absence of crystalline silicates
706 in the diffuse interstellar medium. *Astrophys. J.* **609**, 826–837.
707 Kim, T. H., Tsuchiyama, A., Takigawa, A. and Matsuno, J. (2017) Synthesis of cosmic dust
708 analogue nanoparticles by induction thermal plasma. *Int. Symp. Plasma Chem.*
709 *XXIII*. #780 (abstr.).
710 Kohara S., Suzuya K., Takeuchi K., Loong C. K., Grimsditch M., Weber J. K. R.,
711 Tangeman J. A. and Key T. S. (2004) Glass formation at the limit of insufficient
712 network formers. *Science* **303**, 1649–1652.
713 Koike C., Imai Y., Chihara H., Suto H., Murata K., Tsuchiyama A., Tachibana S. and
714 Ohara S. (2010) Effects of forsterite grain shape on infrared spectra. *The Astrophys.*
715 *J.* **709**, 983.

716 Le Guillou C., Changela H. G. and Brearley A. J. (2015a) Widespread oxidized and
717 hydrated amorphous silicates in CR chondrites matrices: Implications for alteration
718 conditions and H_2 degassing of asteroids. *Earth Planet. Sci. Lett.* **420**, 162–173.
719 Le Guillou C., Dohmen R., Rogalla D., Müller T., Vollmer C. and Becker H. W. (2015b)
720 New experimental approach to study aqueous alteration of amorphous silicates at
721 low reaction rates. *Chem. Geol.* **412**, 179–192.
722 Le Guillou C. and Brearley A. (2014) Relationships between organics, water and early
723 stages of aqueous alteration in the pristine CR3.0 chondrite MET 00426. *Geochim.*
724 *Cosmochim. Acta* **131**, 344–367.
725 Leroux H., Cuvillier P., Zanda B. and Hewins R. H. (2015) GEMS-like material in the
726 matrix of the Paris meteorite and the early stages of alteration of CM chondrites.
727 *Geochim. Cosmochim. Acta* **170**, 247–265.
728 Leshin L. A., Rubin A. E. and McKeegan K. D. (1997) The oxygen isotopic composition of
729 olivine and pyroxene from CI chondrites. *Geochim. Cosmochim. Acta* **61**, 835–845.
730 Ma M., Liu W., Chen Z., Liu Z. and Li B. (2013) Compression and structure of brucite to
731 31 GPa from synchrotron X-ray diffraction and infrared spectroscopy studies. *Am.*
732 *Mineral.* **98**, 33–40.
733 Mäder U., Jenni A., Lerouge C., Gaboreau S., Miyoshi S., Kimura Y., Cloet V., Fukaya M.,
734 Claret F., Otake T., Shibata M. and Lothenbach B. (2017) 5-year chemico-physical
735 evolution of concrete–claystone interfaces, Mont Terri rock laboratory
736 (Switzerland). *Swiss J. Geosci.* **110**, 307–327.

737 Matsumoto M., Tsuchiyama A., Nakato A., Matsuno J., Miyake A., Kataoka A., Ito M.,
738 Tomioka N., Kodama Y., Uesugi K., Takeuchi A., Nakano T., Vaccaro E. (2019)
739 Discovery of fossil asteroidal ice in primitive meteorite Acfer 094. *Sci. Adv.*, **5**,
740 eaax5078.
741 Nakamura-Messenger K., Clemett S. J., Messenger S. and Keller L. P. (2011) Experimental
742 aqueous alteration of cometary dust. *Met. Planet. Sci.* **46**, 843–856.
743 Nied D., Enemark-Rasmussen K., L'Hopital E., Skibsted J. and Lothenbach B. (2016)
744 Properties of magnesium silicate hydrates (M-S-H). *Cement Concrete Res.* **79**, 323–
745 332.
746 Noguchi R. (2012) Hydrothermal alteration experiments of amorphous silicates:
747 implication to aqueous alteration process of carbonaceous chondrites. Ph. D. thesis,
748 Osaka Univ.
749 Nomura K. and Miyamoto M. 1998. Hydrothermal experiments on alteration of Ca-Al-rich
750 inclusions (CAIs) in carbonaceous chondrites: Implication for aqueous alteration in
751 parent asteroids. *Geochim. Cosmochim. Acta* **62**, 3575–3588.
752 Oelkers E. H. (2001) General kinetic description of multioxide silicate mineral and glass
753 dissolution. *Geochim. Cosmochim. Acta* **65**, 3703–3719.
754 Oelkers E. H. and Gislason S. R. (2001) The mechanism, rates and consequences of
755 basaltic glass dissolution: I. An experimental study of the dissolution rates of
756 basaltic glass as a function of aqueous Al, Si and oxalic acid concentration at 25°C
757 and pH = 3 and 11. *Geochim. Cosmochim. Acta* **65**, 3671–3681.

758 Ohnishi I. and Tomeoka K. (2007) Hydrothermal alteration experiments of enstatite:
759 Implications for aqueous alteration of carbonaceous chondrites. *Meter. Planet. Sci.*,
760 **42**, 49–61.
761 Roosz C., Grangeon S., Blanc P., Montouillout V., Lothenbach B., Henocq P., Giffaut E.,
762 Vieillard P. and Gaboreau S. (2015) Crystal structure of magnesium silicate
763 hydrates (M-S-H): The relation with 2: 1 Mg–Si phyllosilicates. *Cement Concrete*
764 *Res.* **73**, 228–237.
765 Roskosz M., Gillot J., Capet F., Roussel P. and Leroux H. (2011) A sharp change in the
766 mineralogy of annealed protoplanetary dust at the glass transition temperature.
767 *Astron. Astrophys.* **529**, A111.
768 Ruiz-Agudo E., Putnis C. V. and Putnis A. (2014) Coupled dissolution and precipitation at
769 mineral–fluid interfaces. *Chem. Geol.* **383**, 132–146.
770 Satoh H., Kimura Y. and Furukawa E. (2018) Direct transmission electron microscopy
771 visualization of the cement reaction by colloidal aggregation of fumed silica. *Ind.*
772 *Eng. Chem. Res.* **57**, 79–83.
773 Schindler M., Michel S., Batcheldor D. and Hochella Jr M. F. (2019) A nanoscale study of
774 the formation of Fe-(hydr) oxides in a volcanic regolith: Implications for the
775 understanding of soil forming processes on Earth and Mars. *Geochim. Cosmochim.*
776 *Acta* **264**, 43–66.
777 Takigawa A., Furukawa Y., Kimura Y., Davidsson B. and Nakamura T. (2019a) Exposure
778 experiments of amorphous silicates and organics to cometary ice and vapor analogs.
779 *Astrophys. J.* **881**, 27.

780 Takigawa A., Kim T. H., Igami Y., Umemoto T., Tsuchiyama A., Koike C., Matsuno J. and
781 Watanabe T. (2019b) Formation of transition alumina dust around asymptotic giant
782 branch stars: Condensation experiments using induction thermal plasma systems.
783 *Astrophys. J. Lett.* **878**, L7.
784 Tomeoka K. and Buseck P. R. (1985) Indicators of aqueous alteration in CM carbonaceous
785 chondrites: Microtextures of a layered mineral containing Fe, S, O and Ni. *Geochim.*
786 *Cosmochim. Acta* **49**, 2149–2163.
787 Tomeoka K. and Buseck P. R. (1988) Matrix mineralogy of the Orgueil CI carbonaceous
788 chondrite. *Geochim. Cosmochim. Acta* **52**, 1627–1640.
789 Valle N., Verney-Carron A., Sterpenich J., Libourel G., Deloule E. and Jollivet P. (2010)
790 Elemental and isotopic (^{29}Si and ^{18}O) tracing of glass alteration mechanisms.
791 *Geochim. Cosmochim. Acta* **74**, 3412–3431.
792 van Boekel R., Min M., Leinert Ch., Waters L. B. F. M., Richichi A., Chesneau O.,
793 Dominik C., Jaffe W., Dutrey A., Graser U., Henning Th., de Jong J., Köhler R., de
794 Koter A., Lopez B., Malbet F., Morel S., Paresce F., Perrin G., Preibisch Th.,
795 Przygodda F., Schöller M. and Wittkowski M. (2004) The building blocks of
796 planets within the 'terrestrial' region of protoplanetary disks. *Nature* **432**, 479–482.
797 Wakabayashi H. and Tomozawa M. (1989) Diffusion of water into silica glass at low
798 temperature. *J. Am. Ceram. Soc.* **72**, 1850–1855.
799 Warren B. E. (1941) X-ray diffraction in random layer lattices. *Phys. Rev.* **59**, 693.

800 Weisberg M. K., Prinz M., Clayton R. N. and Mayeda T. K. (1993) The CR (Renazzo-type)
801 carbonaceous chondrite group and its implications. *Geochim. Cosmochim. Acta* **57**,
802 1567–1586.
803 Yamamoto D. and Tachibana S. (2018) Water vapor pressure dependence of crystallization
804 kinetics of amorphous forsterite. *ACS Earth Space Chem.* **2**, 778–786.
805 Yamazaki T., Kimura Y., Vekilov P. G., Furukawa E., Shirai M., Matsumoto H., Van
806 Driessche A. E. S. and Tsukamoto K. (2017) Two types of amorphous protein
807 particles facilitate crystal nucleation. *P. Natl. Acad. Sci. USA* **114**, 2154–2159.
808 Zhang T., Cheeseman C. R. and Vandeperre L. J. (2011) Development of low pH cement
809 systems forming magnesium silicate hydrate (M-S-H). *Cement Concrete Res.* **41**,
810 439–442.
811 Zolensky M., Barrett R. and Browning L. (1993) Mineralogy and composition of matrix
812 and chondrule rims in carbonaceous chondrites. *Geochim. Cosmochim. Acta* **57**,
813 3123–3148.
814
815

816 **Figure captions**

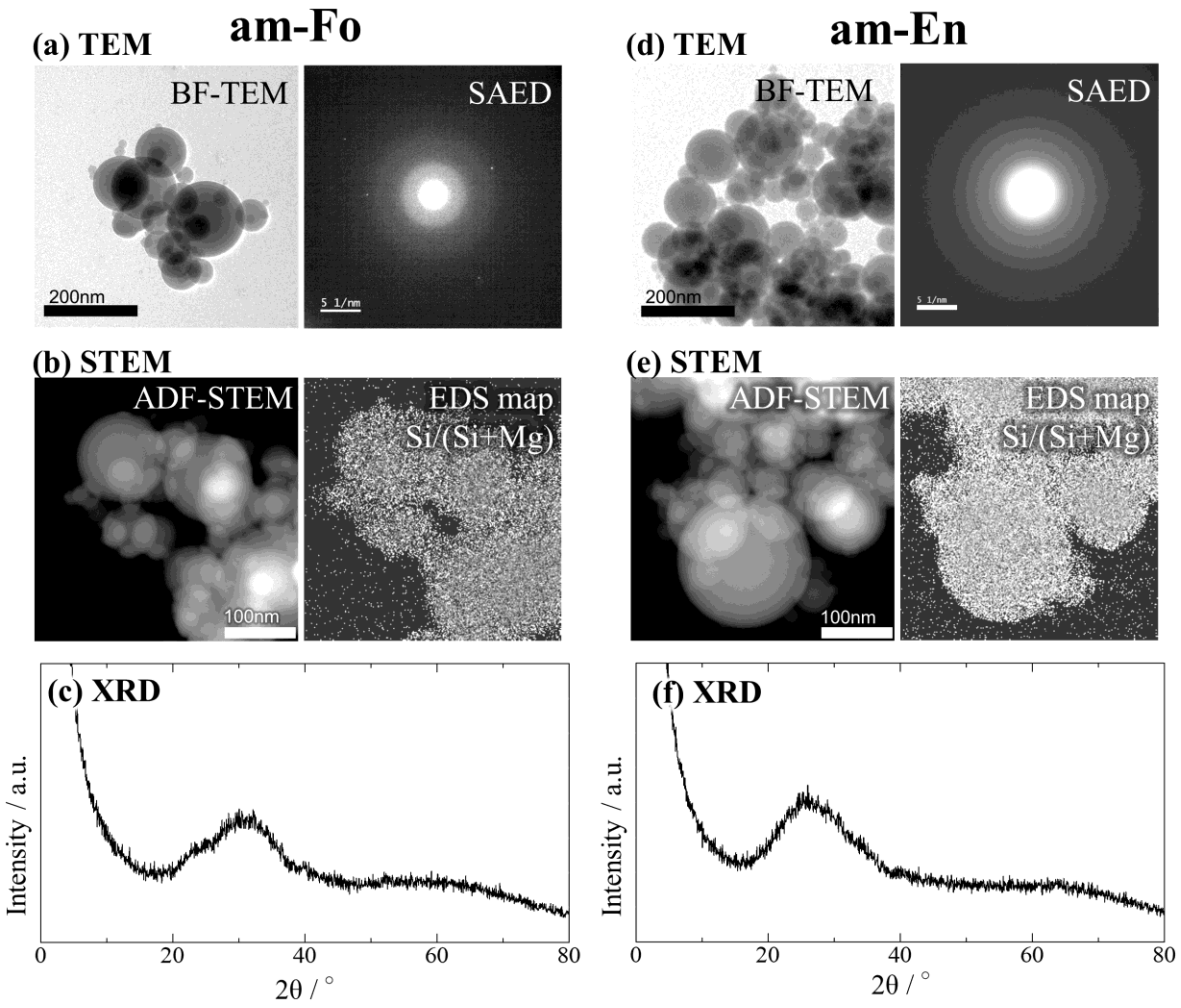

817

818 **Figure 1.**

819 Amorphous silicate particles used as starting materials for am-Fo (MgO/SiO_2 = 2.02). (a)
820 TEM image and SAED pattern, (b) Annular dark-field (ADF)-STEM image and EDS map,
821 and (c) XRD pattern. For am-En (MgO/SiO_2 = 1.15), (d) TEM image and SAED pattern,
822 (e) ADF-STEM image and EDS map, and (f) XRD pattern. The EDS maps show the count
823 ratio for Si-K / (Si-K + Mg-K).

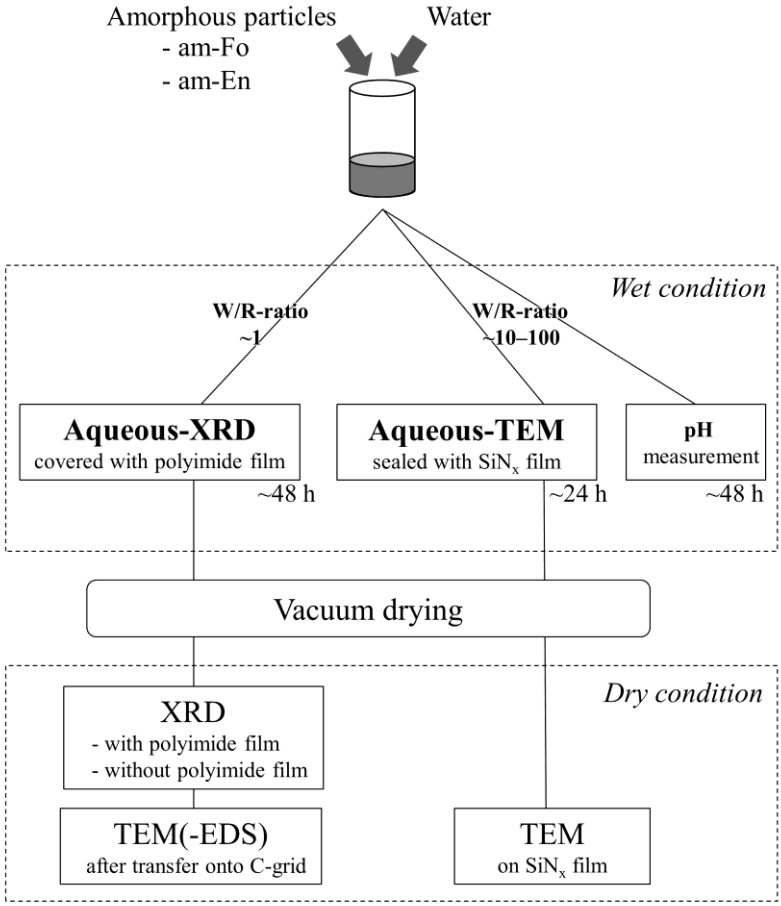

Figure 2.

Schematic of the experimental protocol.

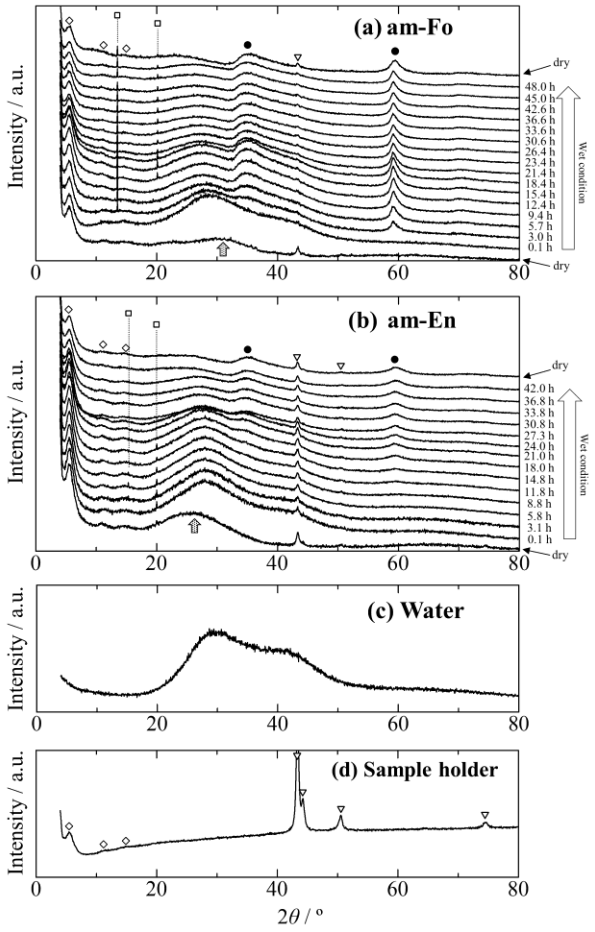

Figure 3.

Time evolution of the XRD patterns obtained successively in the aq-XRD experiments. (a) XRD patterns of am-Fo. (b) XRD patterns of am-En. (c) XRD pattern of water for reference. (d) XRD pattern of the airtight sample holder for reference. In (a) and (b), *in-situ* XRD patterns are shown in order of elapsed time from bottom to top. The plots are offset for convenient analysis. The patterns of the starting materials and of the final run products after drying are also shown at the very bottom and the top of each plot, respectively. These were obtained in dry conditions but covered with a polyimide film and a stainless-steel stage. The *in-situ* patterns are labeled with the time elapsed since the starting material was mixed with water. Peaks in the XRD patterns are marked with the following symbols: polyimide, open diamonds; stainless-steel, open triangles; unknown, open squares; amorphous silicate, arrows; and newly appeared phase (M-S-H), solid circles.

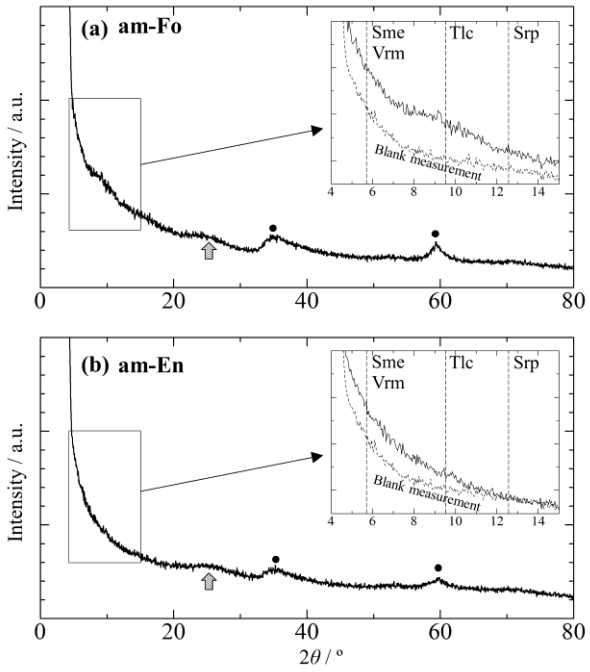

Figure 4.

XRD patterns of the dried run products without the airtight sample holder (polyimide film and stainless-steel holder). (a) am-Fo and (b) am-En. Peaks related to amorphous silicates and M-S-H are indicated by arrows and solid circles, respectively. Each inset is an enlargement of the low-2θ-angle region, where the XRD pattern of a blank measurement that was performed under the same conditions but without a sample is represented by a dotted line. Vertical dotted lines indicate the 2θ positions of the basal reflections of Mg phyllosilicates: Sme, smectite; Vrm, vermiculite; Tlc, talc; and Srp, serpentine.

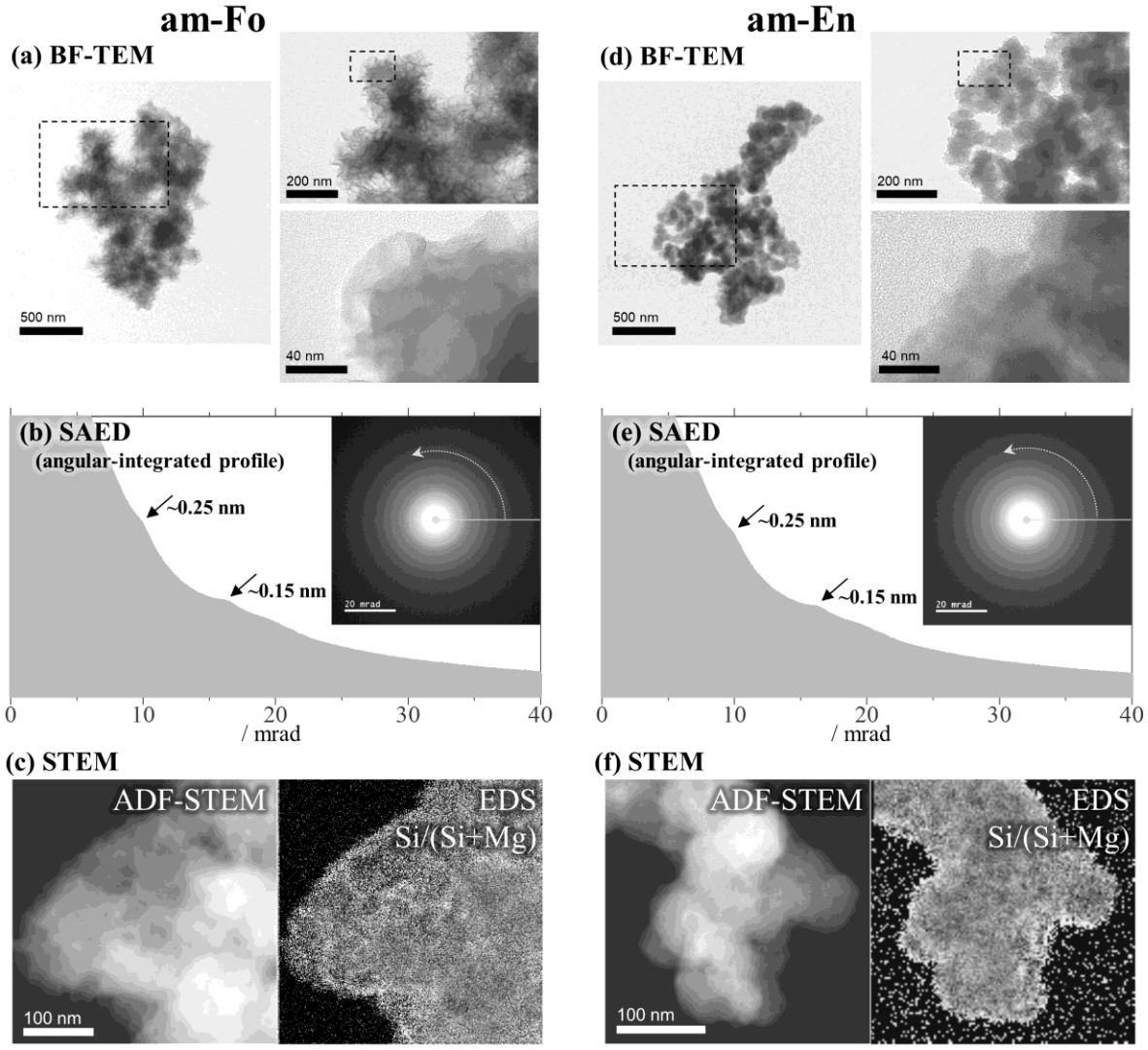

Figure 5.

TEM images and SAED patterns of am-Fo (a–c) and am-En (d–f) after aq-XRD. (a) and (d) TEM images of dried run products. (b) and (e) SAED patterns and their angular-integrated profiles. The broad intensity increases at ~0.25 and ~0.15 nm in *d*-spacing are derived from M-S-H and correspond to the XRD peaks at 35° and 60°, respectively. (c) and (e) ADF-STEM images and EDS maps. The EDS maps show the count ratio of Si-K / (Si-K + Mg-K).

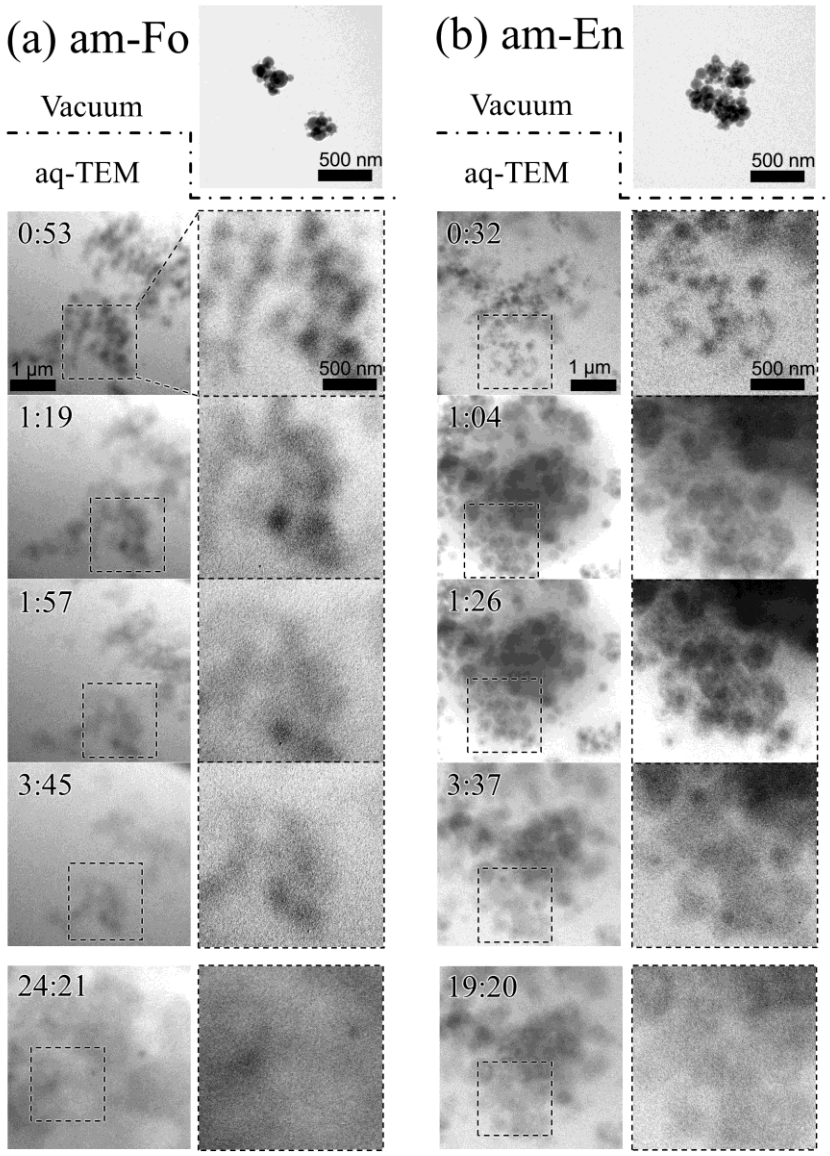

Figure 6.

TEM images of (a) am-Fo and(b) am-En in the aq-TEM experiment. The upper-right panels show the dry starting materials. All other images are *in-situ* images of materials immersed in water. The images in each left column are labeled with the time elapsed (in hours and minutes) since the starting material was mixed with water. The images in each right column are enlargements of the dotted squares in the left images. The magnifications of the images are the same within each column.

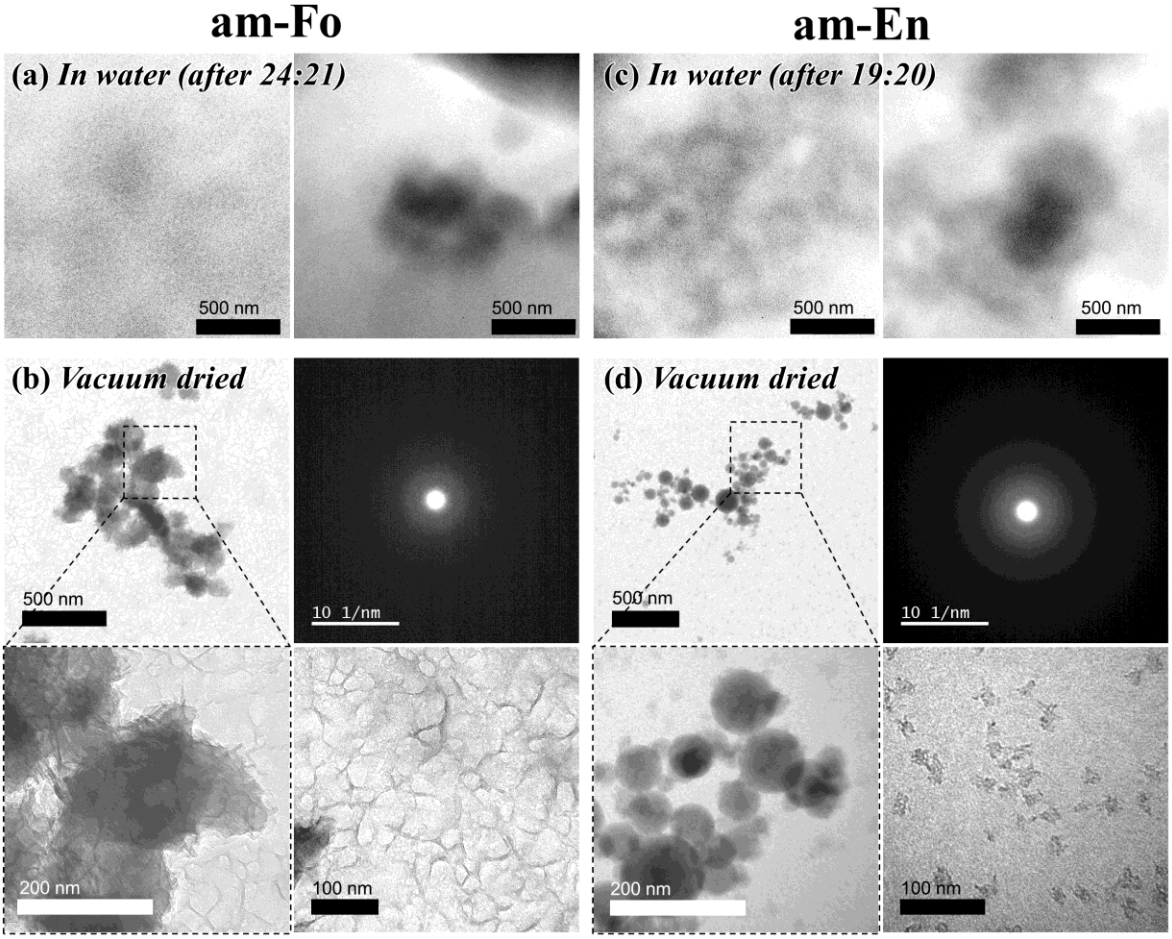

876

877 **Figure 7.**

878 TEM images of am-Fo (a–b) and am-En (c–d) at the end of the aq-TEM experiments. (a)
879 and (c) *In-situ* images at the end of the aq-TEM experiments before removing the sealing.
880 (b) and (d) TEM images and SAED patterns of dried run products after removing the
881 sealing. The upper-right panel shows the SAED pattern obtained from the particles. The
882 lower-left panel is an enlarged image of the particles, and the lower right panels are
883 enlarged images of the SiN_x film floor.

884

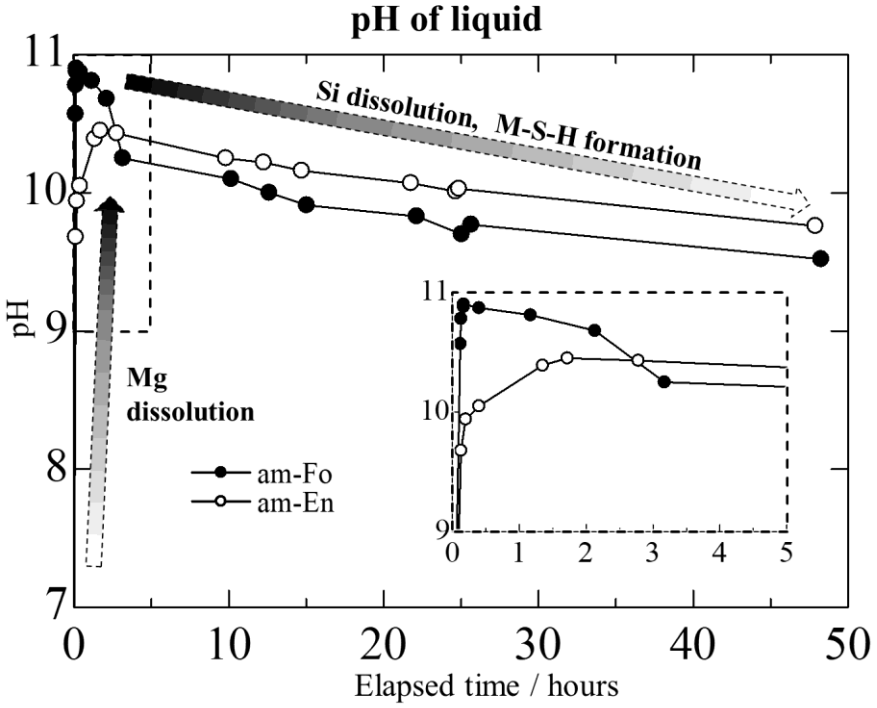

885

886 **Figure 8.**

887 Time evolution of the measured pH values of the water solutions of am-Fo (solid circles)
888 and am-En (open circles). The horizontal axis indicates the time elapsed since the starting
889 material was mixed with water. The inset is an enlargement for the elapsed time period 0–5
890 h and the pH values 9–11. An increase in the pH value is interpreted as resulting from
891 selective dissolution of Mg^{2+} ions from the amorphous silicates, whereas a decrease is
892 interpreted as resulting from subsequent Si^{4+} dissolution and/or M-S-H formation.

893

894

895

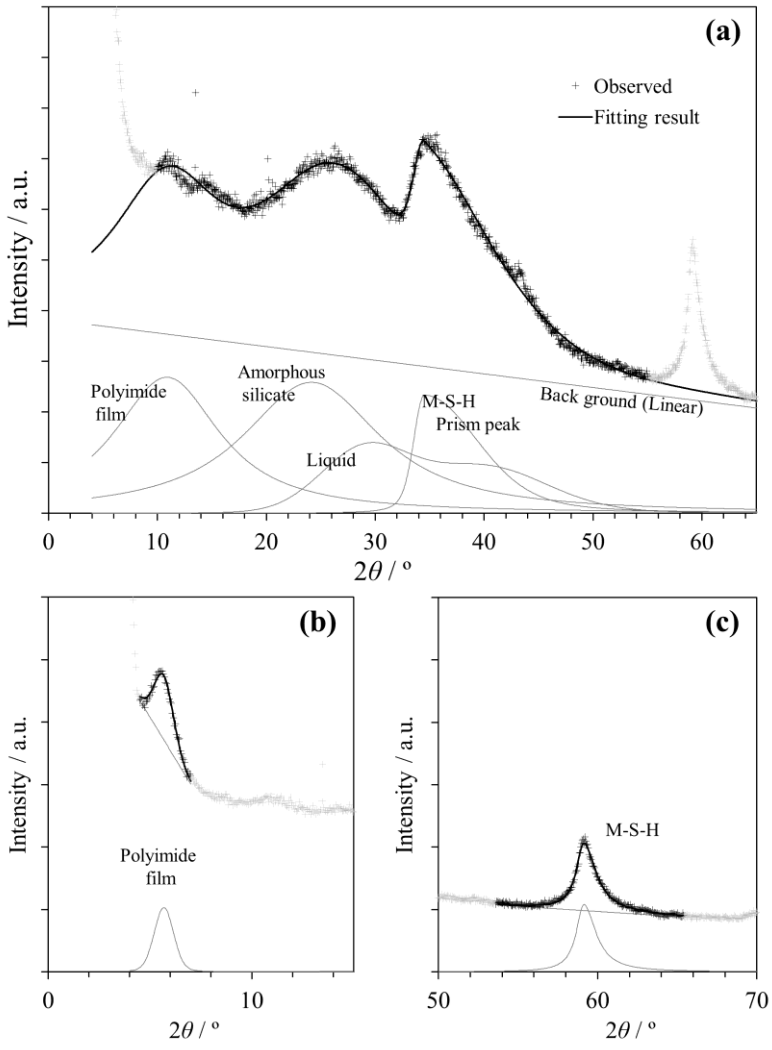

Figure 9.

A typical peak-fitting result for the aq-XRD pattern of am-Fo at 45.0 h after mixing with water. The experimental profile and the fit are shown by crosses and by a black line, respectively. (a) For the 2θ region 10–55°, polyimide film, amorphous silicate, M-S-H, liquid, and a smoothly varying background intensity were assumed (gray lines). The background was assumed to be a linear function. The polyimide intensity (~10°), amorphous peak (~25°), and M-S-H peak (~60°) were fitted with Voigt functions, and the M-S-H prism peak (~35°) was fitted with a split Voigt function. The liquid diffraction profile was assumed to be composed of two Voigt functions, which we determined by fitting to the water diffraction pattern (Fig. 3c). (b) and (c) The polyimide peak at ~6° and the M-S-H peak at ~60° that are out of the range 2θ = 10–55° were fitted individually after subtraction of a linear background.

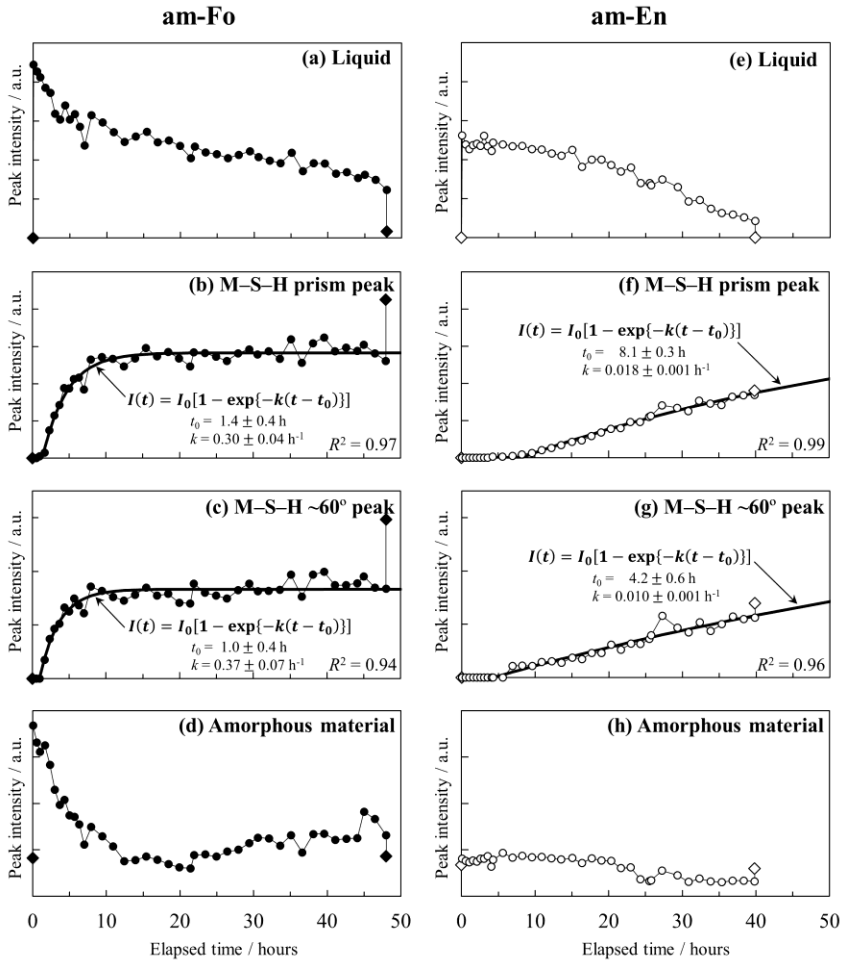

Figure 10.

Time evolution of the intensities of the liquid, M-S-H, and amorphous materials from the *in-situ* XRD patterns of am-Fo (a–d) and am-En (e–h). The intensities are normalized to the polyimide peak intensity at ~6°, which should be independent of the elapsed time. The intensities of the starting materials and the final run products after drying are also shown (diamonds). The horizontal axis indicates the time elapsed since the starting material was mixed with water. (a) and (e) The peak intensity of liquid. (b) and (f) The intensity of the M-S-H prism peak. (c) and (g) The intensity of the M-S-H ~60° peak. (d) and (h) The peak intensity of amorphous material. The solid lines in (b), (c), (f), and (g) are results obtained by fitting with the empirical expression for $I(t)$ given by eq. (1). The optimized parameters t_0 and k and the coefficient of determination R^2 for each fit are also shown in each panel.

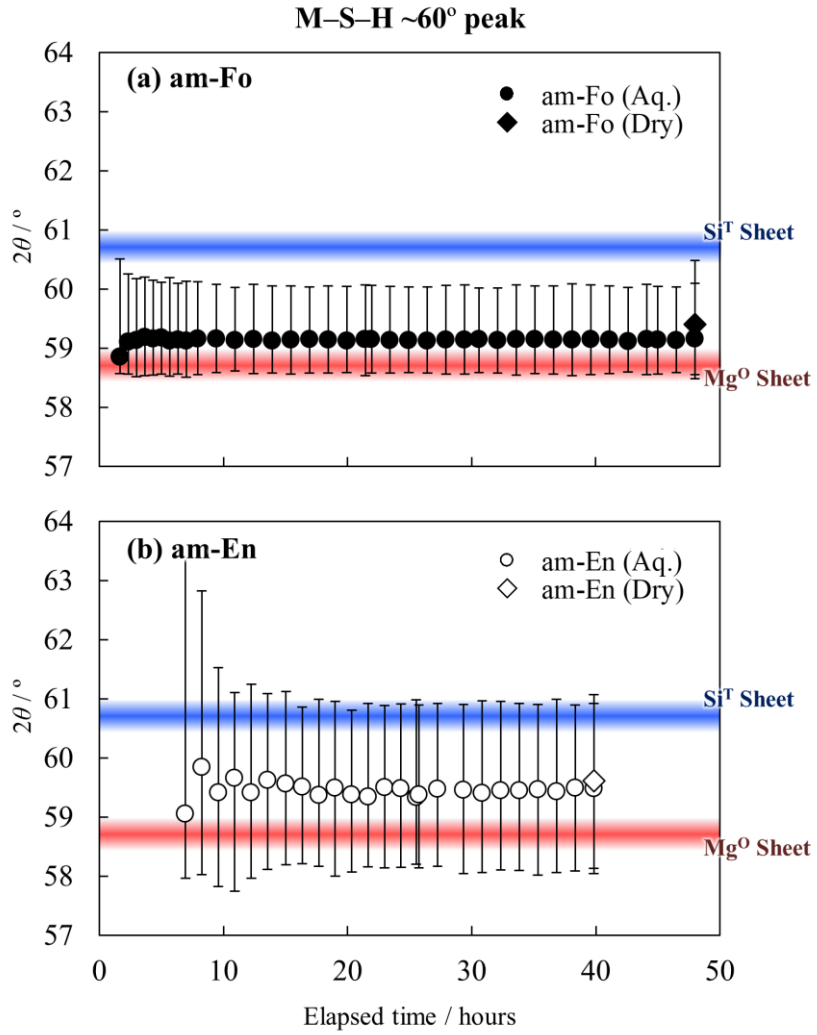

940

941 **Figure 11.**

942 Time evolution of the peak-top position of the M-S-H ~60° peak, with its FWHM
943 determined by fitting with a split Voigt function for am-Fo (a) and am-En (b). Those of the
944 final run products after drying are also shown by diamonds. The horizontal axis indicates
945 the time elapsed since the starting material was mixed with water.

946